# Graphene-Like Conjugated Molecule as Hole-Selective Contact for Operationally Stable Inverted Perovskite Solar Cells and Modules

*Tianhao Wu, Xiushang Xu, Luis K. Ono, Ting Guo, Silvia Mariotti, Chenfeng Ding, Shuai Yuan, Congyang Zhang, Jiahao Zhang, Kirill Mitrofanov, Qizheng Zhang, Saurav Raj, Xiao Liu, Hiroshi Segawa, Penghui Ji, Tongtong Li, Ryota Kabe, Liyuan Han, Akimitsu Narita,\* and Yabing Qi\**

Further enhancing the operational lifetime of inverted-structure perovskite solar cells (PSCs) is crucial for their commercialization, and the design of hole-selective contacts at the illumination side plays a key role in operational stability. In this work, the self-anchoring benzo[*rst*]pentaphene (SA-BPP) is developed as a new type of hole-selective contact toward long-term operationally stable inverted PSCs. The SA-BPP molecule with a graphene-like conjugated structure shows a higher photostability and mobility than that of the frequently-used triphenylamine and carbazole-based hole-selective molecules. Besides, the anchoring groups of SA-BPP promote the formation of a large-scale uniform hole contact on ITO substrate and efficiently passivate the perovskite absorbers. Benefiting from these merits, the champion efficiencies of 22.03% for the small-sized cells and 17.08% for $5 \times 5$ cm$^2$ solar modules on an aperture area of 22.4 cm$^2$ are achieved based on this SA-BPP contact. Also, the SA-BPP-based device exhibits promising operational stability, with an efficiency retention of 87.4% after 2000 h continuous operation at the maximum power point under simulated 1-sun illumination, which indicates an estimated $T_{80}$ lifetime of 3175 h. This novel design concept of hole-selective contacts provides a promising strategy for further improving the PSC stability.

## 1. Introduction

Perovskite solar cells (PSCs) have emerged as a promising photovoltaic technology owing to the unique optoelectronic properties of metal halide perovskite materials, including the strong light-absorption coefficient in the visible-light region, long diffusion length for charge carriers, and solution-based processability suitable for large-area solar modules.[1–3] In recent years, inverted p-i-n structured PSCs with good compatibility for tandem solar cells and lower sensitivity to moisture and oxygen compared to that of the regular n-i-p devices, have made a great improvement on the power conversion efficiency (PCE).[4–7] This large efficiency progress could be attributed to the careful design of interface passivation layer, optimization of perovskite compositions, and development of novel hole-selective contacts.[8–11]

T. Wu, L. K. Ono, T. Guo, S. Mariotti, C. Ding, S. Yuan, C. Zhang,
J. Zhang, P. Ji, T. Li, Y. Qi
Energy Materials and Surface Sciences Unit (EMSSU)
Okinawa Institute of Science and Technology Graduate University (OIST)
1919-1 Tancha, Kunigami-gun, Okinawa, Onna-son 904-0495, Japan
E-mail: Yabing.Qi@OIST.jp
X. Xu, Q. Zhang, S. Raj, A. Narita
Organic and Carbon Nanomaterials Unit
Okinawa Institute of Science and Technology Graduate University
1919-1 Tancha, Kunigami-gun, Okinawa, Onna-son 904-0495, Japan
E-mail: akimitsu.narita@oist.jp

The ORCID identification number(s) for the author(s) of this article can be found under https://doi.org/10.1002/adma.202300169.

K. Mitrofanov, R. Kabe
Organic Optoelectronics Unit
Okinawa Institute of Science and Technology Graduate University
1919-1 Tancha, Kunigami-gun, Okinawa, Onna-son 904-0495, Japan
X. Liu, H. Segawa
Special Division of Environmental and Energy Science
Komaba Organization for Educational Excellence (KOMEX)
College of Arts and Sciences
University of Tokyo
Tokyo 153–8902, Japan
L. Han
State Key Laboratory of Metal Matrix Composites
School of Material Science and Engineering
Shanghai Jiao Tong University
Shanghai 200240, China

**ADVANCED
SCIENCE NEWS**
www.advancedsciencenews.com

**ADVANCED
MATERIALS**
www.advmat.de

Among them, the design of hole-selective contacts at the device illumination side has a strong influence on not only the efficiency but also the long-term operational stability of inverted PSCs, and is currently under intensive investigation.[12–15]

So far, both inorganic metal oxides (such as $NiO_x$, $CuScO_2$, and $CuGaO_2$) and organic semiconductors have been developed as the hole-selective contacts for realizing the high-performance inverted PSCs.[16–18] Particularly, p-type organic semiconductors with low-temperature processibility and tunable energy-level for improved energy alignment with perovskite layer are frequently used. Many aromatic systems with the electron-donating ability, such as triarylamines, carbazoles, and poly-thiophene, have been employed as the π-conjugated building blocks of hole-selective molecules.[19–24] Poly(bis(4-phenyl)(2,4,6-trimethylphenyl)amine) (PTAA) is a commonly-used triarylamine-based hole-selective contact to produce high-performance inverted PSCs with an operational $T_{80}$ lifetime (the time over which the efficiency reduces to 80% of its initial value) of 1000–1500 h.[25,26] However, additional surface modifications are needed to improve the interface quality between PTAA and the perovskite layer when further enlarging the device area.[27,28] To address this issue, Chen et al. developed the PTAA derivative functionalized with pyridine anchoring groups (p-PY) as hole-selective contact,[29] the pyridine groups could form chemical bonding with both the perovskite absorber and ITO glass, which enables a faster hole-extraction process and efficient passivation of the perovskite/hole contact interface (named as the perovskite buried interface in the following discussion). Thanks to these benefits, over 20% PCE and better operational stability were achieved in the 1 cm² p-PY-based device. Besides, the carbazole-based molecules such as 2PACz and MeO-2PACz with a phosphonic acid anchoring group have recently been developed as a conformal hole-selective contact to produce the inverted PSCs with over 21% efficiency,[30] which demonstrated a large application potential on solar modules and textured silicon-perovskite tandem devices. Afterward, additional studies were carried out to improve the device's operational stability by optimizing these carbazole-based self-anchoring molecules. For example, Palomares et al. reported a hole-selective molecule, EADR04, with a π-conjugated linker between the carbazole core and the anchoring group, which led to an estimated $T_{80}$ lifetime of 2086 h for their inverted PSCs.[31] Furthermore, Wu et al. reported a donor-acceptor (D-A) conjugated structure for the hole-selective molecules to improve their intrinsic photostability,[32] where the D-A structure promotes the delocalization of electron cloud from triarylamine or carbazole cores to the strongly electron-withdrawing anchoring groups (such as cyanoacetic acid), which effectively stabilizes the inverted PSCs under operational condition and results in a $T_{95}$ lifetime of 800 h. Although great effort has been made, the operational lifetime of inverted PSCs is still lower than that of their regular counterparts at the current stage. Therefore, a new design concept of hole-selective contacts considering both high photostability and good compatibility for solar modules is urgently needed.

Polycyclic aromatic hydrocarbons (PAHs) have been widely investigated as fascinating organic semiconductors in view of their intriguing graphene-like conjugated structure with tunable optoelectronic properties and promising stability against light and heat.[33,34] PAHs-based semiconductors exhibit promising charge carrier mobility due to their electron delocalization character that results from the large π-extended conjugation structure, further promoting their applications as in advanced optoelectronic devices.[35,36] In general, the properties of PAHs heavily depend on their size, symmetry, and the edge structure. Particularly, benzo[rst]pentaphene (BPP, the chemical structure of a tert-butyl derivative used in this work is shown in **Figure 1**a) with a combination of zigzag and armchair edges can be an excellent platform to tune the energy levels for discovering novel hole-selective contacts toward high-performance PSCs.[37,38] Moreover, the facile synthesis and modification of BPP deserve attention in the fabrication of large-area solar modules.

In this work, we develop the hole-selective molecule with the BPP core and the methyl benzoate terminal groups that spontaneously anchor on the ITO substrate and perovskite buried interface (namely self-anchoring benzo[rst]pentaphene, SA-BPP) for operationally stable inverted PSCs and modules. Experimental results and theoretical calculations demonstrate that SA-BPP can form a suitable energy-level alignment with perovskite absorber to extract photo-generated holes, and its self-anchoring property enables a better defect passivation capability at the perovskite buried interface compared to that of BPP. X-ray photoelectron spectroscopy (XPS) and in situ mass spectrometry (MS) analyses suggest that SA-BPP and its passivated perovskite interface show better stability than that of the triphenylamine-based PTAA and carbazole-based MeO-2PACz reference samples under continuous 1-sun illumination. Moreover, SA-BPP can be used for upscalable fabrication of the PSCs, which enables the champion efficiencies of 22.03% for small-sized cells and 17.08% for 5 × 5 cm² solar modules on an aperture area of 22.4 cm². The SA-BPP-based small-sized cells and modules retained 87.4% and 88.5% of their initial PCEs after continuous operation under simulated 1-sun illumination for 2000 and 1000 h (estimated $T_{80}$ lifetimes of 3175 and 1739 h), respectively, which are among the longest operational stability reported for the inverted PSCs so far.

## 2. Results and Discussion

### 2.1. Molecule and Film Characterization

Synthesis details of SA-BPP are summarized in Figure S1 (Supporting Information) and the experimental section. The BPP core was synthesized through the "dehydrative π-extension" (DPEX) reaction according to a previously reported procedure,[39] and the tert-butyl groups were installed to increase the solubility of BPP in organic solvents to realize the use of solution deposition method. SA-BPP was synthesized through regioselective bromination of BPP with N-bromosuccinimide (NBS),[40] followed by the Suzuki–Miyaura coupling reaction with 4-(methoxycarbonyl)phenylboronic acid. The structures of BPP and SA-BPP were characterized by nuclear magnetic resonance (NMR) spectroscopy (see Figures S2 and S3, Supporting Information for further details) and high-resolution mass spectrometry (HRMS, Figure S4, Supporting Information). Both BPP and SA-BPP show no detectable impurity peak
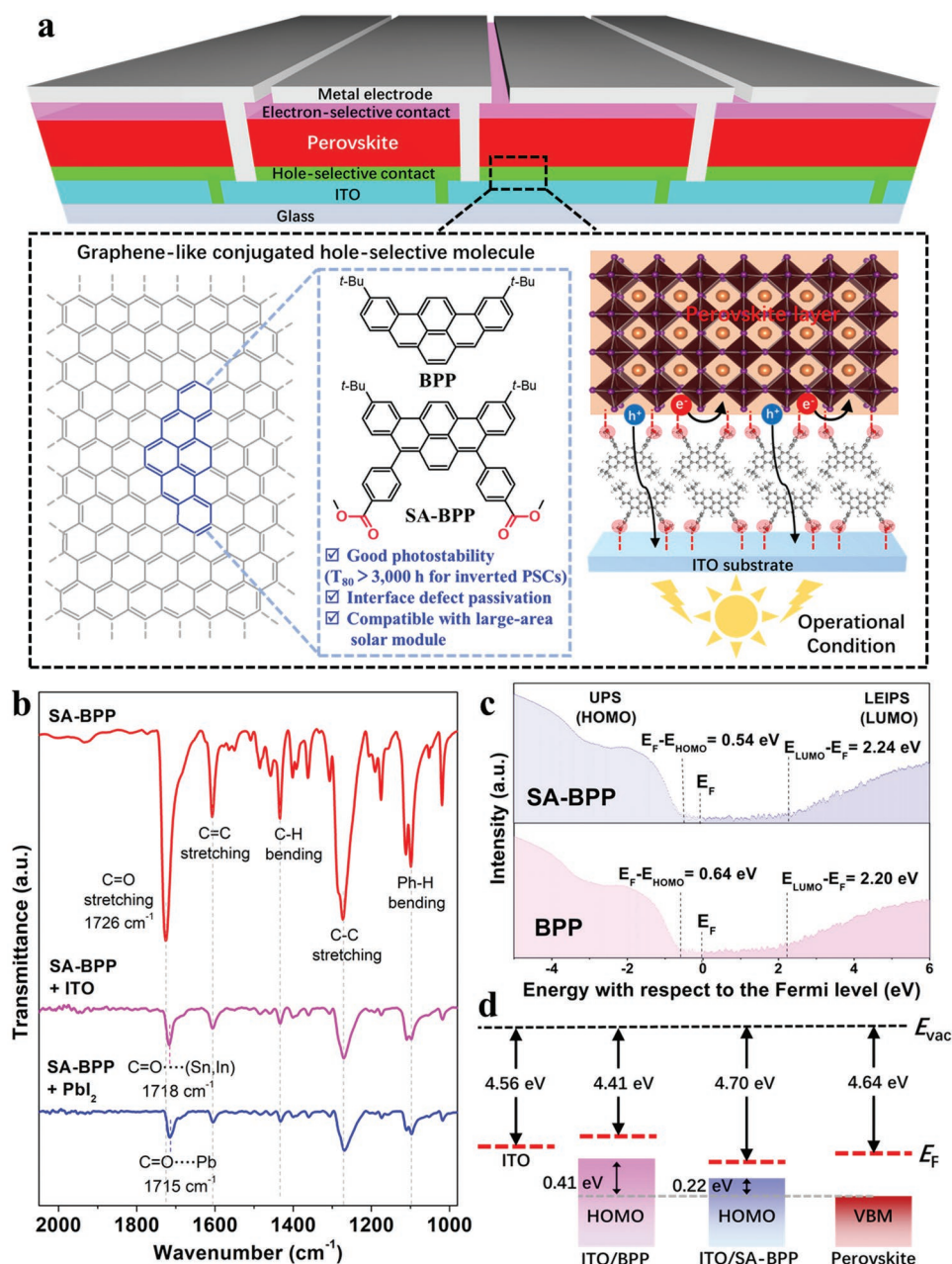
**Figure 1.** Properties of the graphene-like hole-selective molecules. a) Chemical structures of the BPP and SA-BPP molecules, and the schematic illustration of the SA-BPP hole-selective contact that could form the bonding with both the ITO substrate and perovskite layer in the inverted PSCs. b) FTIR spectra of the pure SA-BPP, SA-BPP-ITO mixture, and SA-BPP-PbI$_2$ mixture. c) Band structures of the BPP and SA-BPP films coated on ITO substrate determined by the UPS and LEIPS measurements. d) Energy offset between the HOMO of BPP and SA-BPP, and the VBM of perovskite absorber, the red dash line indicates the $E_F$ position.

in their NMR spectra, indicating high purity of the synthesized products. Particularly, SA-BPP powder could be easily dissolved in the green solvents such as the commonly-used ethyl acetate, which enables the open-air fabrication of the SA-BPP hole-selective contact for the solar module production.

We first performed density functional theory (DFT) calculations to reveal the distribution of the frontier molecular orbitals of BPP and SA-BPP. As can be seen in Figure S5 (Supporting Information), both the highest occupied molecular orbital (HOMO) and the lowest unoccupied molecular orbital (LUMO)

cover the fused six-membered benzenoid rings of BPP, indicating a strong delocalization of the electron cloud. In the case of SA-BPP, both the HOMO and LUMO are partially extended to the electron-withdrawing benzoate terminal groups. As demonstrated by the previous study, such delocalized frontier orbital distribution can significantly improve the photostability of the organic semiconductors.[32]

To reveal the band structure of these graphene-like molecules, we performed the UV photoemission spectroscopy (UPS) and low-energy inverse photoemission spectroscopy

**ADVANCED
SCIENCE NEWS**

www.advancedsciencenews.com

**ADVANCED
MATERIALS**

www.advmat.de

(LEIPS) to measure the HOMO and LUMO positions with respect to the Fermi level ($E_F$). As demonstrated in Figure 1c, the energy gaps between HOMO and LUMO were calculated to be 2.84 and 2.78 eV for BPP and SA-BPP, respectively, and the SA-BPP molecule shows a more *p*-type characteristic. From the secondary electron cutoff feature of UPS spectra (Figure S6, Supporting Information),[41] we can determine the ionization potential of the BPP and SA-BPP to be 5.05 and 5.24 eV, respectively, which suggests an energy offset of 0.41 and 0.22 eV with respect to the valence band maximum (VBM) of the perovskite film (cesium-formamidinium-methylammonium lead iodide ($CsFAMAPbI_3$) was used in this work). Such a deeper HOMO level of SA-BPP could be attributed to the decreased electron density on the BPP core caused by the electron-withdrawing benzoate terminal groups. Besides, the deeper $E_F$ position of SA-BPP compared to the BPP and pure ITO enables a barrier-free hole extraction process from perovskite absorber to the hole contact (Figure 1d).

Then, we characterized the interaction between SA-BPP molecule and ITO or perovskite components using Fourier transform infrared (FTIR) spectroscopy. As shown in Figure 1b, the pure SA-BPP samples show the IR absorption features at 1726 $cm^{-1}$ (C=O stretching vibration), 1605 $cm^{-1}$ (C=C stretching vibration), 1438 $cm^{-1}$ (C—H bending vibration), 1282 $cm^{-1}$ (C—C stretching vibration), and 1099 $cm^{-1}$ (Ph—H (the C—H bond on phenyl rings) bending vibration). The C=O vibration peak of SA-BPP shifts to a lower wavenumber with respect to the C—C and C—H peaks after being mixed with ITO or $PbI_2$, indicating the formation of C=O····Pb bonding with the $PbI_2$ or C=O····(Sn and In) bonding with the ITO that changes the chemical environment of the C=O group.[42]

Furthermore, we investigated the self-anchoring behaviors of BPP and SA-BPP molecules on the $In_2O_3$ (100) surface (simulating the ITO) through the DFT method. MeO-2PACz frequently used for fabricating the high-performance inverted PSCs was chosen as a reference sample. As can be seen in Figure S7a (Supporting Information), strong coupling of the electron cloud between the phosphonic acid group and the surface In atom could be found in $In_2O_3$ (100)/MeO-2PACz sample, and the adsorption energy ($E_{ads}$) was calculated to be −2.15 eV, but the BPP molecule showed a very small $E_{ads}$ of −0.34 eV on $In_2O_3$ (100) surface due to the lack of anchoring group. By contrast, the SA-BPP molecule/$In_2O_3$ (100) interface generated two obvious charge-redistribution sites owing to the bonding formed between the C=O groups and the In atoms on $In_2O_3$ surface, resulting in a much larger $E_{ads}$ of −2.61 eV. On the other hand, we also simulated the anchoring effect of SA-BPP on the perovskite surface, and a pure $FAPbI_3$ slab was used for the calculation process. As demonstrated in Figure S7b (Supporting Information), the SA-BPP molecule shows a similar adsorption behavior on the $FAPbI_3$ (100) surface with the charge redistribution on its two C=O groups, resulting in a larger $E_{ads}$ than that of the BPP and MeO-2PACz molecules. Additionally, we investigated the surface wettability for different hole-selective contacts (Figure S8, Supporting Information). The contact angles with N,N-dimethylformamide (DMF) were measured to be 19.5°, 64.1°, and 20.4° for MeO-2PACz, BPP, and SA-BPP films, respectively, indicating good surface wettability of SA-BPP and MeO-2PACz for depositing

perovskite solution. The much larger contact angle in the case of the BPP film can be attributed to its hydrophobic property.

To visualize the uniformity of the hole-selective thin film coated on ITO glass, a surface-sensitive technique, scanning Kelvin probe microscopy (SKPM) was applied to achieve the surface potential mapping profiles of different hole-selective contacts on a $50 \times 50$ $\mu m^2$ region. As depicted in **Figure 2**a–c, the BPP film shows a clear green (low potential) and red (high potential) regions in the mapping profile, while the SA-BPP film shows a uniform color mapping with a smaller difference between the minimum and the maximum potential values than that of the BPP and MeO-2PACz films. A possible explanation is that the double-site anchoring effect of the SA-BPP molecule leads to a more ordered loading on the ITO surface. On the contrary, the heterogeneous potential distribution of BPP film could be attributed to the intermolecular aggregation induced by strong π-π interaction. Also, the relative atomic force microscopy (AFM) morphological images (Figure S9, Supporting Information) indicate a lower root-mean-square (RMS) roughness of the SA-BPP film (2.75 nm) compared to that of the BPP (6.59 nm) and MeO-2PACz (3.06 nm) films.

Scanning electron microscope (SEM) measurement was conducted to study the morphology of perovskite films deposited on different hole-selective contacts. As shown in Figure 2d–f, the perovskite films deposited on MeO-2PACz and SA-BPP exhibited a smoother surface morphology compared with the perovskite film grown on BPP. Also, surface potential mapping profiles ($50 \times 50$ $\mu m^2$) of the perovskite films deposited on SA-BPP showed a much lower potential fluctuation than that of the perovskite films coated on BPP and MeO-2PACz (Figure S10a–c, Supporting Information). Moreover, the average grain sizes of the MeO-2PACz/perovskite, BPP/perovskite, and SA-BPP/perovskite films were estimated to be 391, 382, and 394 nm (Figure S10d–f, Supporting Information), respectively, indicating that the perovskite grain size is not strongly affected by different hole-selective contacts. On the other hand, cross section SEM images (Figure 2g–i) indicate a pinhole-free contact for the ITO/MeO-2PACz/perovskite and ITO/SA-BPP/perovskite samples, while a random orientation of the perovskite grains with many pinholes was found at the BPP/perovskite interface, which usually leads to a non-radiative recombination of the charge carriers.

Next, the crystal structures of perovskite films were characterized by X-ray diffraction (XRD) measurement. Figure S11 (Supporting Information) depicts the XRD patterns of different samples, the perovskite film on BPP substrate showed a weaker peak intensity of the (100) and (200) crystal planes that are crucial for the charge carrier transport in perovskite absorber compared to the XRD patterns of SA-BPP/perovskite or MeO-2PACz/perovskite samples. The above results illustrate that the strong chemical bonding between hole-selective contact and perovskite buried interface is crucial for the growth of compact and highly oriented perovskite crystals.

## 2.2. Interface Charge Carrier Dynamics

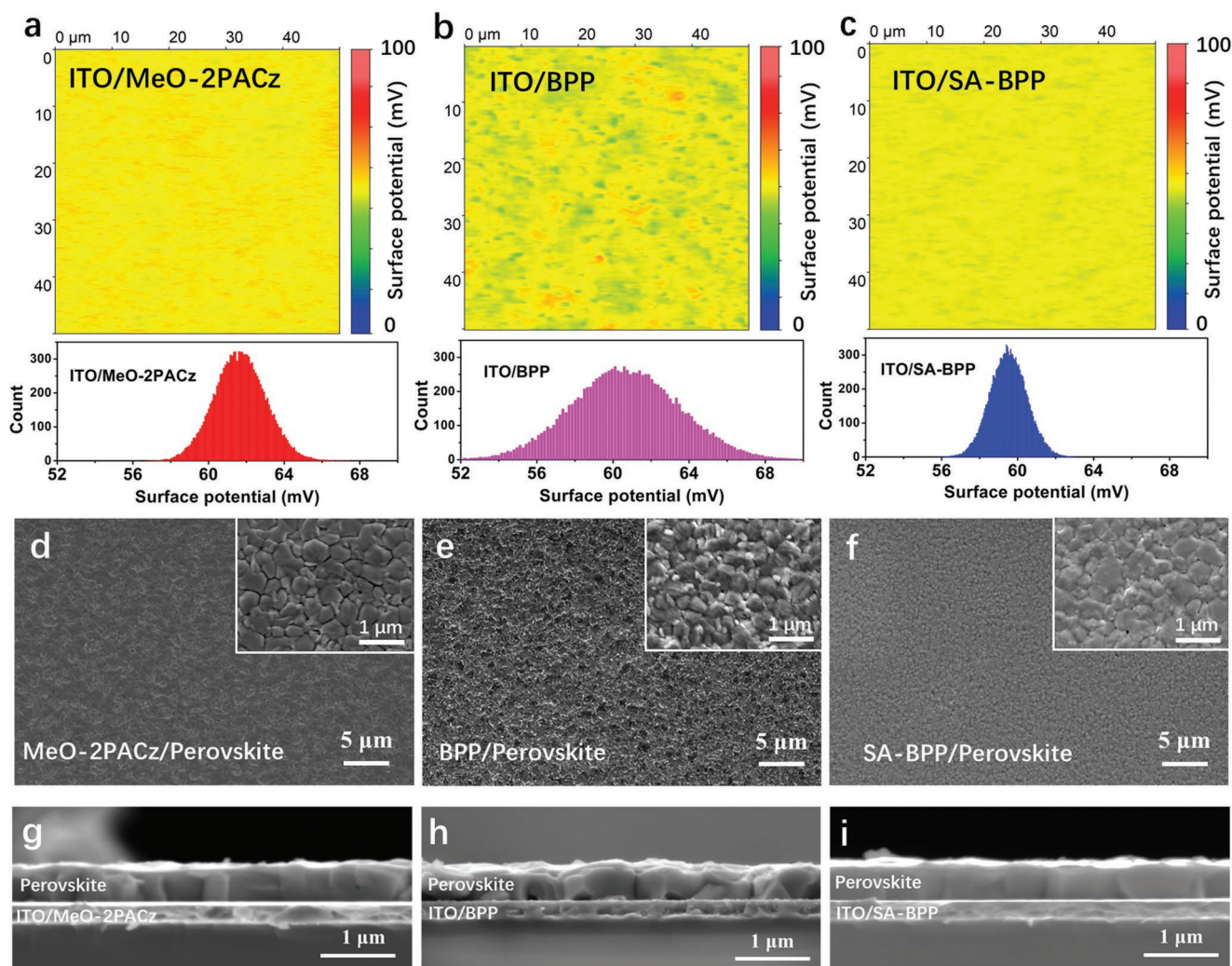Additionally, we further investigated the interface carrier dynamics through femtosecond transient absorption

**Figure 2.** Uniformity of hole-selective contacts and subsequently-deposited perovskite films. a–c) Surface potential mapping profiles on a $50 \times 50 \ \mu m^2$ region for a) the ITO/MeO-2PACz, b) ITO/BPP, and c) ITO/SA-BPP samples. The potential statistical distributions are also shown to indicate the homogeneity of these thin films. d–f) Top-view SEM images of the perovskite films deposited on d) MeO-2PACz, e) BPP, and f) SA-BPP hole-selective contacts. g–i) Cross section SEM images of the perovskite films deposited on g) MeO-2PACz, h) BPP, and i) SA-BPP hole-selective contacts.

spectroscopy (TAS) technique. Sample structures of glass/hole-selective contacts/perovskite layer were employed for TAS measurements. As shown in **Figure 3**a–c, a unique ground-state bleaching (GSB) peak of the CsFAMAPbI$_3$ perovskite was formed at ≈749 nm, and the quenching process of the GSB peak was detected at the pump-probe delay time from 30 to 500 ps. The quenching rate of GSB peak indicates the carrier transport efficiency from perovskite absorber to hole contact.[43,44] A larger quenching of over 95% of GSB peak intensity was found in the SA-BPP/perovskite film under 500 ps delay time compared to that of MeO-2PACz/perovskite (81%) and BPP/perovskite (64%) films, reflecting a high hole extraction efficiency at the SA-BPP/perovskite interface. We also note that the TAS curve of SA-BPP/perovskite film with 30 ps delay time shows a wider GSB peak range, which could be attributed to the uneven baseline induced by the noise of our homemade pump-probe system. Then, we calculated the decay lifetimes of GSB peak to be 103.2, 146.5, and 80.1 ps

for MeO-2PACz/perovskite, BPP/perovskite, and SA-BPP/perovskite, respectively, by fitting the decay kinetics plots of TAS spectra (Figure S12, Supporting Information). Details of the fitting parameters are summarized in Table S1 (Supporting Information).

Moreover, the uniformity of the charge extraction process at hole contact interface was investigated through photoluminescence (PL) mapping technique. Figure 3d–f shows the PL mapping profiles of the corresponding samples on a $100 \times 100 \ \mu m^2$ region, the blue color region indicates a strong PL quenching while the red color region indicates a weak PL quenching. The MeO-2PACz/perovskite and BPP/perovskite samples show a heterogeneous PL mapping intensity, reflecting a large difference of the charge extraction behaviors. Such differences of PL characteristics at the micro-scale region could be ascribed to the heterogeneity of perovskite morphology and hole contact quality. By contrast, the PL mapping profile of SA-BPP/perovskite demonstrates a more uniform hole
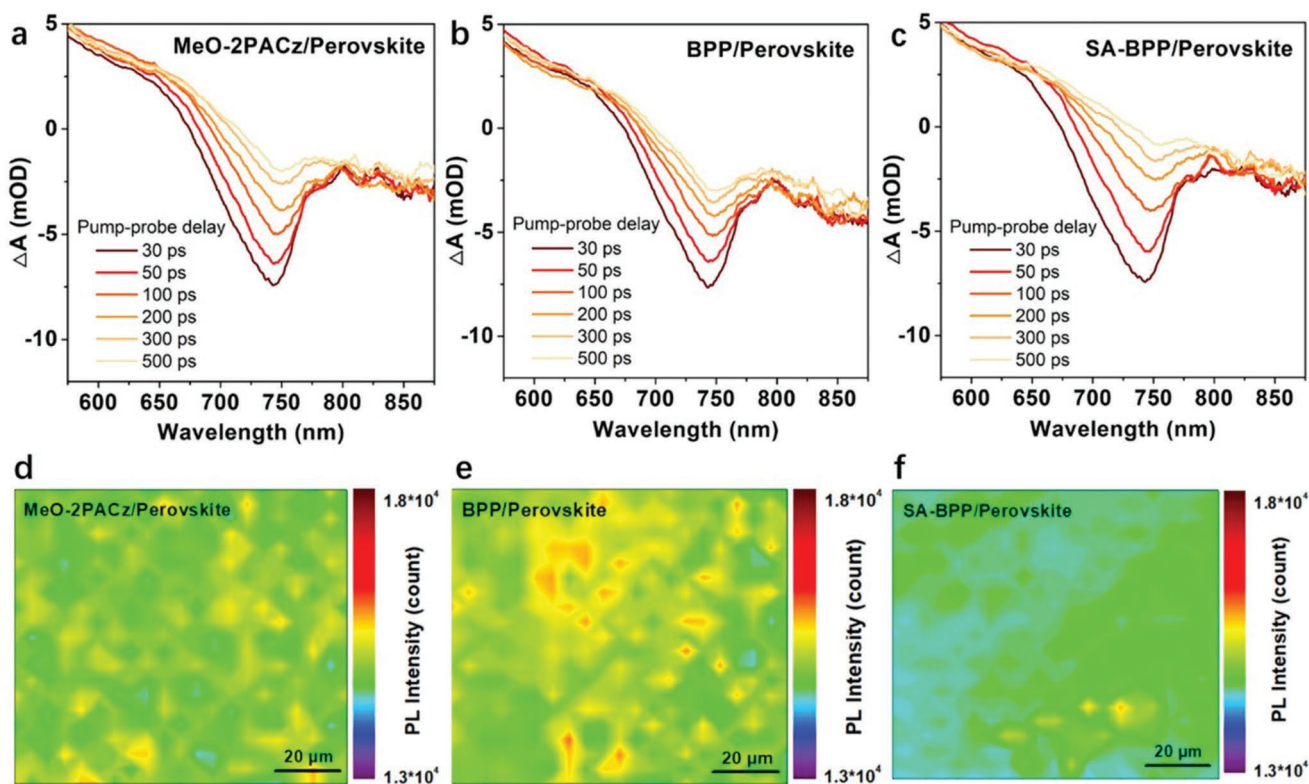
**Figure 3.** Carrier dynamics at the hole-selective contact/perovskite interface. a–c) Delay time-dependent transient absorption spectra at the pump-probe delay time of 30–500 ps for a) the MeO-2PACz/perovskite, b) BPP/perovskite, and c) SA-BPP/perovskite films deposited on the glass substrate. d–f) PL mapping profiles on a $100 \times 100~\mu m^2$ region of the perovskite films deposited on d) the MeO-2PACz, e) BPP, and f) SA-BPP substrates.

extraction process, which is crucial for realizing an efficient charge carrier separation in the large-area device.

Generally, the charge extraction process is highly affected by the carrier mobility ($\mu_h$). In this regard, we estimated the hole mobility ($\mu_h$) of different hole-selective contacts by calculating the slope of the dark current density-voltage$^2$ ($J$–$V^2$) plot according to the Mott–Gurney equation.[45] Here, the hole-only devices containing MeO-2PACz or SA-BPP layer were employed for measuring the $J$–$V^2$ plots (Figure S13a,b, Supporting Information). The $\mu_h$ of SA-BPP is calculated to be $(4.27 \pm 0.29) \times 10^{-4}~cm^2~V^{-1}~s^{-1}$, which is 6 times higher than that of MeO-2PACz ($\mu_h = (7.12 \pm 0.15) \times 10^{-5}~cm^2~V^{-1}~s^{-1}$), and also higher than that of the undoped PTAA or spiro-OMeTAD ($\mu_h \approx 10^{-5}~cm^2~V^{-1}~s^{-1}$) reported by previous studies.[11,46]

Besides the mobility, the trap density ($N_{trap}$) at the perovskite buried interface should also be an important factor to determine the hole extraction efficiency. In this work, the $N_{trap}$ value was measured by the space charge limit current (SCLC) method, and the results were summarized in Figure S13c (Supporting Information). The dark current plots of the hole-only devices with a structure of ITO/hole-selective contact/perovskite/Au show an Ohmic regime (slope $n = 1$), a trap-filled limited regime (TFL, $n > 3$) and a trap-free SCLC regime (Child, $n = 2$), the $N_{trap}$ can be derived from the onset voltage ($V_{TFL}$) of TFL regime according to their linear correlation.[47] The $N_{trap}$ values of the MeO-2PACz, BPP, and SA-BPP-based samples were estimated to be $7.95 \times 10^{15}$, $9.93 \times 10^{15}$, and $6.34 \times 10^{15}~cm^{-3}$, respectively, indicating the fact that SA-BPP is

able to minimize the trap states and thus enables fast extraction of the photogenerated hole in perovskite absorber.

We further uncovered the passivation mechanism of the SA-BPP contact via simulating the interaction between SA-BPP or BPP molecules and the iodide vacancy that has been regarded as the main source of defects for iodide-based perovskite materials,[48] and a pure cubic FAPbI$_3$ perovskite model was applied here to simplify the calculation process. Figure S14 (Supporting Information) illustrates the density of state (DOS) distribution of the FAPbI$_3$ (100) slabs without and with the passivation of SA-BPP or BPP, and the insets show the corresponding geometry-optimized structures with an iodide vacancy on the surface (indicated by blue circle). The pristine FAPbI$_3$ slab shows a localized charge distribution of the HOMO orbital, which generates additional trap states at both valence and conduction band edges, resulting in recombination of the electrons and holes. These calculation results are consistent with the previous ab initio analysis of the defect-containing perovskite structure.[49] In the case of BPP-passivated FAPbI$_3$ slab, the trap states are still presented at band edges owing to the weak electronic coupling between the BPP core and the surface under-coordinated Pb cations. In contrast, the chemical bonding between the C=O groups of SA-BPP and surface under-coordinated Pb cations effectively delocalizes the charge distribution around the Pb—I frameworks, which minimizes the trap density at the valence and conduction band edges in SA-BPP-passivated FAPbI$_3$ model.

## 2.3. Stability of Hole-Selective Contact and Relative Interface

For a systematical comparison, we further investigated the stability of SA-BPP hole-selective contact under continuous 1-sun illumination, and the frequently-used carbazole-based MeO-2PACz and triphenylamine-based PTAA were used as reference samples. The evolution of their XPS C 1s core levels before and after the aging process can be seen in **Figure 4**a–c. Note that the XPS peak intensity decay of the aged sample was indicated by the percentage numbers with respect to the initial peak intensity of the fresh sample, and the same XPS fitting model for both fresh and aged spectra was applied here. The separated peaks at 284.5, 285.3, 286.2, and 287.3 eV are associated with the C−C (C=C), C−N, C−O−C, and C−P bonds of the MeO-2PACz, respectively.[30] It was found that the intensity of C−N and C−P peaks decreased to 72% and 75% of the initial values, respectively, after aging at 1-sun illumination for 100 h, indicating a degradation of the carbazole core and phosphonic acid group. In contrast, no obvious change of the C−C, C−O−C, and O=C−O peak intensities for SA-BPP sample (Figure 4b) was found, reflecting that the BPP core and the benzoate terminal group kept stable after aging at the same condition. Besides, the PTAA contact also showed a severe light-induced degradation of the triphenylamine unit, the intensity of C−N peak decreased to 68% of the initial value after aging process (Figure 4c).

Also, the conductive atomic force microscope (C-AFM) measurement was performed to study the impact of structure evolutions on the conductivity of these hole-selective contact. As shown in Figure S15 (Supporting Information), the C-AFM current mapping profiles of MeO-2PACz film show a significant drop of the average current from 1.68 to 0.81 nA after aged at 1-sun illumination for 100 h under the same applied bias, and the mapping current of the PTAA film showed a similar decay trend (from 1.62 to 1.19 nA). By contrast, a negligible change of the mapping current (0.17 nA) could be found in the SA-BPP film after aging process. The above results highlight the excellent photostability of the SA-BPP with respect to the MeO-2PACz and PTAA benchmarks.

Besides the hole-selective contact itself, the relative perovskite buried interface also play a critical role in the long-term operational stability of inverted PSCs. In situ mass spectrometry (MS) technique is a power tool for the stability study, which can identify the gas-phase degradation products and reveal their partial pressure evolution under the influence of light and heat. This technique was applied in our previous studies for revealing the temperature-dependent or light-dependent degradation mechanisms of the perovskite materials and their relative interfaces.[50,51] Here in this work, we employed such an MS system to track the released degradation products from the hole-selective contact/perovskite interface under simulated 1-sun illumination in a vacuum chamber with a background pressure of $10^{-8}$ Torr. The schematic diagram of this in situ MS system is illustrated in Figure S16a (Supporting Information). Figure 4d–f shows the MS contour plots with the mass-to-charge ratio (m/z) of 1–200 amu for the perovskite films deposited on MeO-2PACz, SA-BPP, and PTAA substrates, and the possible degradation pathways derived from the MS plots were summarized in Figure 4g. The degradation products with a m/z

of 17, 27, 31, 44, 73, 127/128, and 142 amu were detected after being exposed to 1-sun light, associated with the $NH_3^+$, $HCN^+$, $CH_3NH_2^+$ (MA gas), $CH(N_2H_3)^+$ (FA gas), $DMF^+$ (*N,N*-dimethylformamide solvent), $I^+/HI^+$ (hydrogen iodide), and $CH_3I^+$ (methyliodide), respectively. Also, the fragments induced by the ionization process of mass analysis were detected, including $CH_3^+$ (m/z = 15, methyl group), $NH_2^+$ (m/z = 16, amino group), $CH_4N^+$ (m/z = 30, MA fragment), $CH_2N_2^+$ (m/z = 42, FA fragment), and $I^{2+}$ (m/z = 63, iodide fragment). The generation of gas-phase FA, MA, and HI could be attributed to the deprotonation reaction of organic ammonium components. The deprotonation process can be accelerated under continuous illumination or elevated temperature, as illustrated by the increased partial pressure of the corresponding components. Differently, the formation of $NH_3$, HCN, and $CH_3I$ was induced by the thermal decomposition of $CH(N_2H_3)$ and the reaction between $CH_3NH_2$ and HI according to previous reports.[52] As shown in Figure S16b–d (Supporting Information), in the case of MeO-2PACz/perovskite, the partial pressure of $NH_3$, $CH_3NH_2$, $CH(N_2H_3)$, and HI increased by 3–4 times after 120 min of illumination, and the partial pressure of $CH_3NH_2$ and $CH(N_2H_3)$ increased by about one order of magnitude for the PTAA/perovskite sample. By contrast, less degradation products were released from the SA-BPP/perovskite sample, which means that the deprotonation and decomposition of organic components in perovskite absorber could be effectively suppressed under operational conditions, which could be attributed to the good perovskite crystal quality induced by the SA-BPP contact as well as the enhanced interface stability.

To further illustrate the possible reason for the stability improvement at perovskite buried interface, we calculated the electrostatic potential (ESP) profiles of MeO-2PACz, SA-BPP, and PTAA based on the DFT method (Figure S17a, Supporting Information). For the MeO-2PACz and PTAA models, negative ESP (indicated by red color) mainly locates at the electron-rich carbazole unit and the benzene rings of triphenylamine unit, while a much higher electron density at the BPP core of SA-BPP could be found. The high electron density at BPP core could be attributed to the strong delocalized effect of the $\pi$ electrons and is able to provide the active sites for forming cation-$\pi$ interactions with the FA$^+$ or MA$^+$ cations. As demonstrated in Figure S17b (Supporting Information), the interaction energy between SA-BPP molecule and a FA$^+$ cation is calculated to be −1.08 eV, much higher than that of the MeO-2PACz-FA$^+$ (−0.47 eV) or PTAA-FA$^+$ (−0.28 eV) complex.[53] Such cation-$\pi$ interaction is able to fix the volatile organic cations at the perovskite buried interface and thus suppress the light-induced degradation of perovskite crystal under operational conditions.

## 2.4. Device Performance and Stability

We fabricated the inverted planar PSCs with a structure of ITO/SA-BPP/perovskite (500–550 nm)/PCBM/$C_{60}$/BCP/Ag (**Figure 5**a) to study the impact of SA-BPP on the photovoltaic performance, the MeO-2PACz, and BPP were used as the reference hole-selective contacts for a comprehensive comparison. Figure 5b plots the *J–V* curves of the small-sized PSCs with an aperture area of 0.1 cm$^2$ based on different hole-selective
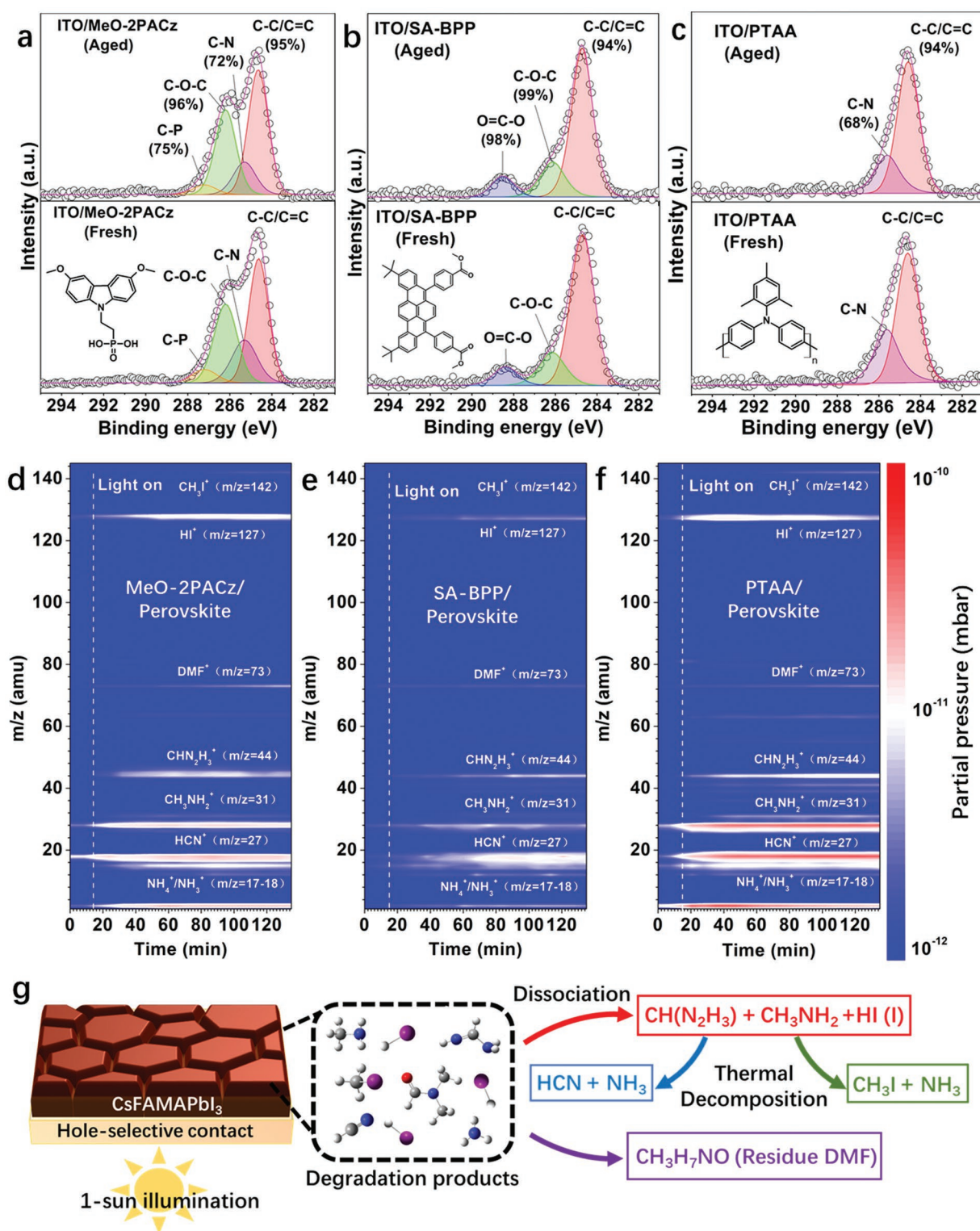
**Figure 4.** Photostability of the hole-selective contacts and the interfaces with perovskite layer. a–c) High-resolution XPS spectra of the C 1s region for the a) MeO-2PACz, b) SA-BPP, and c) PTAA solid-state films coated on ITO substrate before and after being exposed to simulated 1-sun light for 100 h in dry $N_2$, the exact peak intensity decay after aging with respect to the initial value is also indicated. d–f) In situ MS contour profiles (m/z = 1–200 amu) of d) the MeO-2PACz/perovskite, e) SA-BPP/perovskite, and f) PTAA/perovskite films coated on the ITO glass. The simulated 1-sun light was applied after 15 min of MS measurement and the total illumination time was 120 min. g) Possible degradation mechanisms at the perovskite/hole-selective contact interface under 1-sun illumination condition.
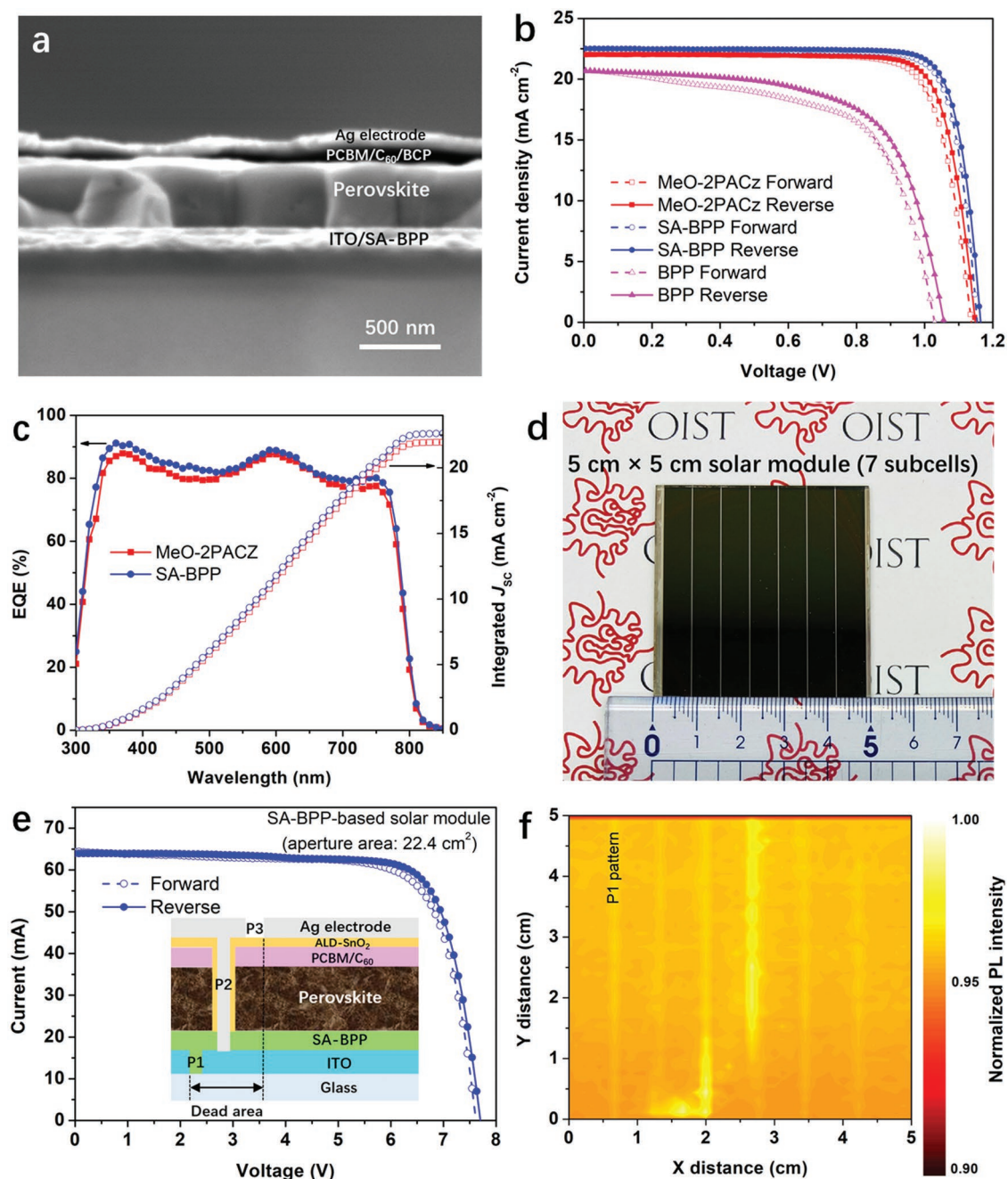
**Figure 5.** Photovoltaic performance of inverted PSCs and modules. a) Cross section SEM image of the SA-BPP-based inverted PSCs. b) J–V curves of the small-sized inverted PSCs (champion device) based on the MeO-2PACz, BPP, and SA-BPP hole-selective contacts. c) EQE spectra of the MeO-2PACz and SA-BPP-based champion devices. d) Photographs of the $5 \times 5$ cm² solar module based on SA-BPP hole-selective contact. e) J–V curves of the SA-BPP-based solar module on an aperture area of 22.4 cm², the inset shows the module architecture with P1, P2, and P3 patterns. f) PL intensity mapping profile of the perovskite film coated on the $5 \times 5$ cm² ITO (with P1 pattern)/SA-BPP substrate.

contacts, and the photovoltaic parameters of the champion devices were summarized in **Table 1**. The MeO-2PACz devices provide the best PCE of 20.57% (reverse scan), with an open-circuit voltage ($V_{OC}$) of 1.15 V, short-circuit current density ($J_{SC}$) of 22.11 mA cm⁻², and fill factor (FF) of 80.89%. By contrast, SA-BPP devices show an obvious improvement on the photovoltaic performance and present the best PCE up to 22.03%,

with a $V_{OC}$ of 1.17 V, $J_{SC}$ of 22.55 mA cm⁻², and FF of 83.50%. On the contrary, a relatively low PCE of 14.51% was obtained by the BPP devices, with a $V_{OC}$ of 1.06 V, $J_{SC}$ of 20.65 mA cm⁻², and FF of 66.31%. In this regard, we attributed the efficiency improvement of SA-BPP devices to the fast hole extraction process, efficient passivation of the perovskite buried interface, and the high mobility of the large-conjugation SA-BPP

**ADVANCED
SCIENCE NEWS**

www.advancedsciencenews.com

**ADVANCED
MATERIALS**

www.advmat.de

**Table 1.** The best photovoltaic performance of the small-sized cells and solar modules based on different hole-selective contacts.

| Hole-selective contact | Scan direction | $J_{SC}$ [mA cm$^{-2}$] | $V_{OC}$ [V] | FF [%] | PCE [%] |
|---|---|---|---|---|---|
| MeO-2PACz | forward | 22.14 | 1.14 | 79.78 | 20.14 |
| | reverse | 22.11 | 1.15 | 80.89 | 20.57 |
| SA-BPP | forward | 22.57 | 1.16 | 82.09 | 21.49 |
| | reverse | 22.55 | 1.17 | 83.50 | 22.03 |
| BPP | forward | 20.71 | 1.03 | 63.18 | 13.48 |
| | reverse | 20.65 | 1.06 | 66.31 | 14.51 |
| SA-BPP (22.4 cm$^2$ solar module) | forward | 2.88 | 7.59 | 75.06 | 16.41 |
| | reverse | 2.87 | 7.68 | 77.51 | 17.08 |

molecule. Also, the reproducibility of the SA-BPP devices is higher than the reference samples in view of the narrower statistical distribution of the photovoltaic parameters (Figure S18, Supporting Information).

Moreover, the external quantum efficiency (EQE) spectra of the corresponding PSCs were investigated, as depicted in Figure 5c. We found that the EQE at the short wavelength region of 350–480 nm increased significantly when an SA-BPP hole-selective contact was incorporated. This EQE enhancement was associated with the improvement in carrier extraction efficiency at the illumination side (perovskite buried interface), which further supports the results from TAS and PL measurements. The integrated $J_{SC}$ derived from EQE spectra were calculated to be 22.08 and 22.49 mA cm$^{-2}$ for the MeO-2PACz and SA-BPP devices, respectively, consistent with the $J_{SC}$ derived from J–V measurements.

To evaluate the potential of SA-BPP for the large-scale production of inverted PSCs, we extended our study to the 5 × 5 cm$^2$ solar module consisting of 7 perovskite subcells connected in series (Figure 5d). The deposition methods of different functional layers are similar to that of the small-sized cells, including the SA-BPP contact (spin-coating), perovskite absorbers (spin-coating), electron-selective contact (evaporation), and Ag electrode (evaporation). The architecture of solar module is illustrated in Figure 5e, and the corresponding pattern design is shown in Figure S19a (Supporting Information). The geometrical fill factor (GFF) was calculated to be 95.8% according to the width of subcell and the dead area between P1 and P3 (Figure S19b, Supporting Information). Besides, a conformal and compact tin oxide layer was deposited atop the P2 pattern via atomic layer deposition (ALD) technique. This ALD-SnO$_2$ layer was applied to prevent the direct contact between iodide-based perovskite absorber and Ag electrode that is able to accelerate the degradation of inverted PSC module under light and heat conditions.[54]

For SA-BPP-based solar module, the corresponding J–V curves (Figure 5e) show a reverse-scan PCE of 17.08% on an aperture area of 22.4 cm$^2$ (active area PCE of 17.83%), with a $V_{OC}$ of 7.68 V, $J_{SC}$ of 2.87 mA cm$^{-2}$, and FF of 77.51%. Regarding the MeO-2PACz-based solar module, a relatively low PCE of 14.77% was obtained (active area PCE of 15.42%), with a $V_{OC}$ of 7.48 V, $J_{SC}$ of 2.81 mA cm$^{-2}$, and FF of 70.28% (Figure S20a and Table S2, Supporting Information). Large-area PL mapping technique was also employed to check the uniformity of the perovskite films deposited on 5 × 5 cm$^2$ substrate. As can be

seen in Figure 5f, the perovskite film coated on 5 × 5 cm ITO/SA-BPP substrate enabled a more uniform PL mapping intensity than that of the film coated on ITO/MeO-2PACz substrate (Figure S20b, Supporting Information), the bright lines of mapping profiles indicate a relatively weak PL quenching effect at the P1 pattern of ITO glass. Also, photographs of the 5 × 5 cm$^2$ perovskite films were illustrated in Figure S20c (Supporting Information).

Furthermore, we evaluated the operational stability of the PSC small-sized cells and modules under accelerated-aging conditions based on the International Summit on Organic Photovoltaic Stability (ISOS) protocols, a home-designed test system was used for the stability measurement (Figure S21a, Supporting Information), and a xenon white light source was employed to simulate the solar irradiation (the spectrum is shown in Figure S21b, Supporting Information). **Figure 6**a demonstrated the normalized PCE decay curves of the unencapsulated PSCs based on MeO-2PACz, SA-BPP, and PTAA hole-selective contacts measured under 1-sun illumination at 45 °C (ISOS-L-2I), and the decay plots with actual PCE values were presented in Figure S22 (Supporting Information). The reference MeO-2PACz and PTAA devices (the cross section SEM image and J–V curves were provided in Figure S23, Supporting Information) showed a normalized PCE decrease of over 20% after continuous operation for 622 and 1030 h, respectively. By contrast, the SA-BPP devices showed a linear-shape PCE decay plot and kept ≈87.4% of the initial efficiency after 2000 h operation, which translates into a $T_{80}$ lifetime of 3175 h which is among the highest operational lifetimes for the inverted PSCs. As a comparison, the operational lifetimes reported by the state-of-the-art devices were summarized in Table S3 (Supporting Information). It is worth noting that the average PCE decay rates of MeO-2PACz and PTAA devices measured in our study have similar trends to the previously reported values, which strongly confirms the reliability of our stability measurement. Besides, we further evaluated the stability reproducibility of the SA-BPP devices by tracking the PCE decay profiles of 6 individual cells (Figure S24, Supporting Information) under the same condition. All the devices exhibited a similar PCE decay rate between 0.0037% per hour and 0.0041% per hour in an operational time of 500 h.

The operational stability of solar modules is one of the most important issues for the commercialization of PSCs. In this regard, we tracked the PCE decay of 5 × 5 cm$^2$ inverted PSC modules versus the operational time in Figure 6b (ISOS-L-2I).
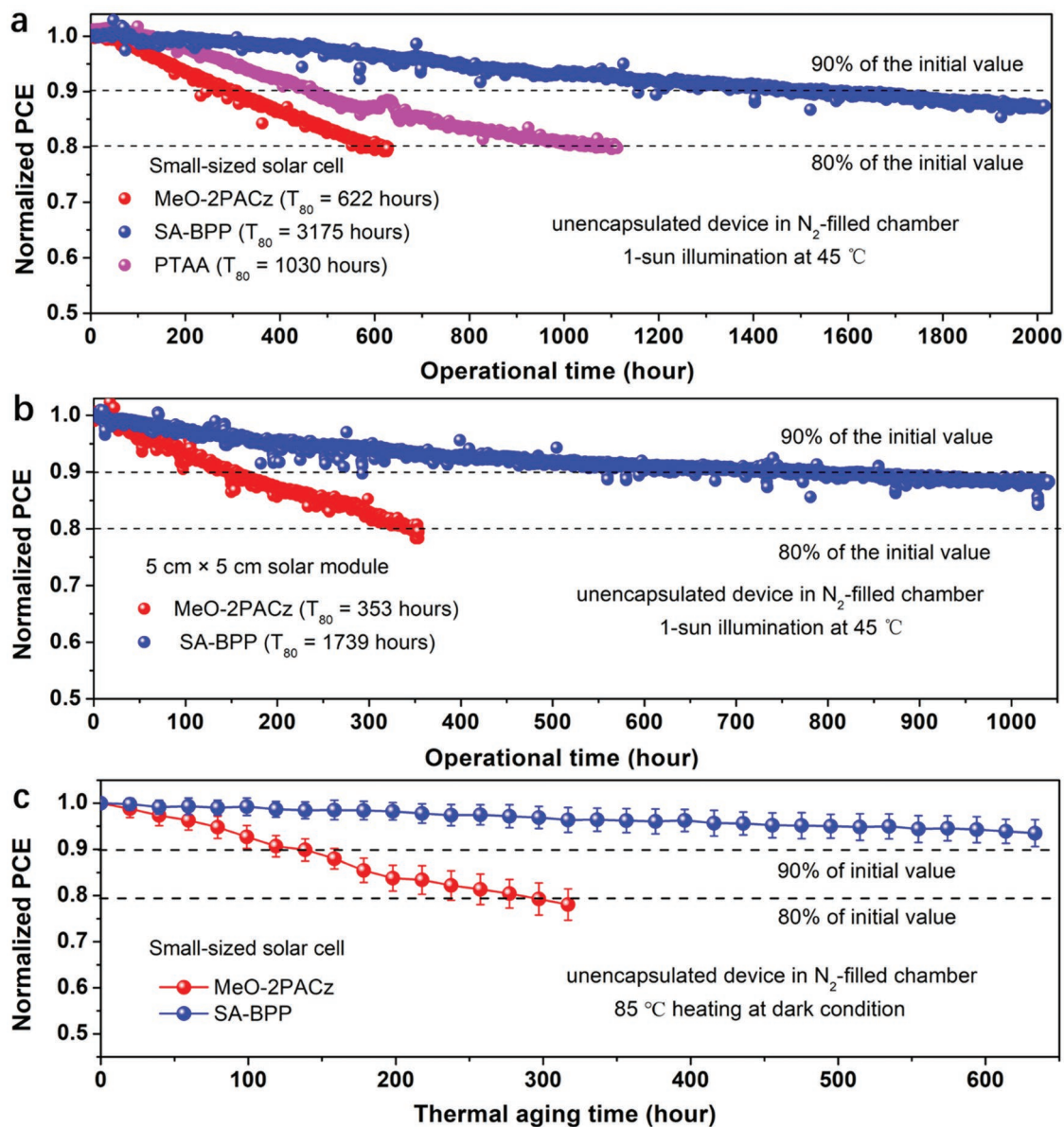
**Figure 6.** Stability of inverted PSCs and modules. a,b) Operational stability tests of the champion devices in an $N_2$-filled chamber at 45 °C for the a) small-sized solar cells and b) 5 × 5 cm² solar modules measured under a constant bias close to the initial maximum power point. c) Thermal stability tests of small-sized solar cells based on the statistical performance of 5 devices.

The SA-BPP-based module retained 88.5% of the initial efficiency after operation for 1000 h, which enables a much longer estimated $T_{80}$ lifetime of 1739 h compared to that of the MeO-2PACz-based module (353 h). Furthermore, the thermal stability of the solar cell devices was investigated, and the results can be found in Figure 6c. The SA-BPP-based inverted PSCs kept over 93% of the initial PCE after being aged at 85 °C for 600 h, while the MeO-2PACz-based devices showed a PCE loss of more than 20% after being aged for 300 h. These results confirm that the graphene-like structure improves the thermal stability of hole-selective contacts and inverted PSCs.

Although the SA-BPP serving as a new type of hole-selective contact has endowed significant stability improvement of the inverted PSCs, we could still find a large stability gap between the small-sized cells and solar modules, which is mainly attributed to the degradation at the connection regions (P2 and P3 patterns) during the long-term operation process. In this work, we try to deposit a compact ALD-SnO₂ layer to suppress the reaction between Ag electrode and the iodide-based perovskite induced by the lateral ion diffusion. The XPS high-resolution O 1s (Figure S25a, Supporting Information) and Sn 3d (Figure S25b, Supporting Information) spectra indicate the formation of tin oxide on the electron-selective contact (PCBM/C₆₀) surface. From the optical microscope images (Figure S25c, Supporting Information), we found that the corrosion of Ag electrode at the edge of P2 and P3 under 1-sun illumination could be retarded when this ALD protection layer was applied, which emphasizes that construction of the compact ion-diffusion

barrier and the development of novel encapsulation materials are key strategies to realize a robust module stability.

## 3. Conclusions

In summary, we propose a novel strategy to design the photo-stable and scalable hole-selective contact based on graphene-like BPP-based molecules toward the long-term stable inverted PSCs. The SA-BPP contact enables a fast and uniform hole extraction process and stabilizes the organic components at the perovskite buried interface. These advantages lead to a higher device efficiency than that of the frequently-used triphenylamine and carbazole-based hole-selective contacts and enable an extrapolated $T_{80}$ operational lifetime of 3175 and 1739 h for the small-sized solar cells and the $5 \times 5$ cm$^2$ perovskite solar modules. More importantly, this work provides in-depth insights into the interface chemistry between perovskite and organic semiconductors, which could be extended to other types of optoelectronic devices in future studies.

## 4. Experimental Section

*Synthesis Details*: All reactions working with air- or moisture-sensitive compounds were carried out under argon atmosphere using standard Schlenk line techniques. Thin-layer chromatography (TLC) was done on silica gel-coated aluminum sheets with F254 indicator and column chromatography separation was performed with silica gel (particle size 0.063–0.200 mm). BPP and 5,8-dibromo-2,11-di-*tert*-butylbenzo[*rst*] pentaphene (A6) were synthesized as recently described.[55] Briefly, 2-bromo-4-(*tert*-butyl)-1-iodobenzene (A2) was prepared by Sandmeyer reaction of 2-bromo-4-(*tert*-butyl)aniline (A1), followed by selective halogen–metal exchange to generate a corresponding Grignard reagent, which was then reacted with DMF to afford aldehyde (A3). Suzuki–Miyaura coupling of A3 with diboronic ester (A4) gave dialdehyde (A5), which was subjected to DPEX reaction to afford BPP. Next, BPP was brominated by NBS to give A6. SA-BPP was finally obtained by Suzuki–Miyaura coupling of A6 and 4-(methoxycarbonyl)phenylboronic acid. The chemical structure of SA-BPP was characterized by the NMR spectroscopy and HRMS.

For the synthesis of SA-BPP, a 100-mL Schlenk tube was charged with A6 (50.0 mg, 0.0877 mmol), 4-(methoxycarbonyl)phenylboronic acid (66.0 mg, 0.263 mmol), tris(dibenzylideneacetone)dipalladium(0) (Pd$_2$(dba)$_3$) (4.00 mg, 4.38 µmol), 2-dicyclohexylphosphino-2″,6″-dimethoxybiphenyl (SPhos) (3.60 mg, 8.77 µmol), K$_3$PO$_4$ (118 mg, 0.556 mmol), and anhydrous toluene (2 mL) under argon atmosphere. The reaction mixture was subjected to freeze-pump-thaw cycles (three times) and heated at 105 °C for 20 h under argon atmosphere. After the resulting mixture was cooled to room temperature and poured into water (20 mL), the organic layer was separated, and the aqueous layer was extracted with CH$_2$Cl$_2$ (10 mL) for three times. The separated organic phases were combined, washed with brine, dried over anhydrous MgSO$_4$, and evaporated. The residue was purified by silica gel column chromatography (eluent: hexane: EtOAc = 10:1) to give SA-BPP (45.5 mg, 76% yield) as light yellow solid. $^1$H NMR (400 MHz, CD$_2$Cl$_2$) $\delta$ 9.41 (s, 2H), 9.16 (d, $J$ = 1.9 Hz, 2H), 8.30–8.16 (m, 4H), 7.77 (dd, $J$ = 8.8, 1.8 Hz, 2H), 7.70 (dd, $J$ = 8.8, 0.5 Hz, 2H), 7.60–7.51 (m, 4H), 7.27 (s, 2H), 3.98 (s, 6H), 1.58 (s, 18H). $^{13}$C NMR (101 MHz, CD$_2$Cl$_2$) $\delta$ 166.85, 149.26, 144.24, 134.19, 131.49, 129.58, 128.71, 128.20, 126.97, 126.79, 126.14, 125.37, 124.49, 122.14, 118.42, 52.08, 35.33, 31.21. HRMS (ESI, Positive): 682.3078 [M]$^+$, found: 682.3093.

*Fabrication of Small-Sized PSCs*: The ITO glass substrate was sequentially washed with distilled water, isopropanol, and acetone. After being dried by N$_2$ flow, the substrate was treated by the UV light (UV)/O$_3$ for 40 min. After that, the hole-selective layers were deposited on the ITO substrate by spin-coating 0.003 M precursor solutions (ethyl alcohol for MeO-2PACz, ethyl acetate for SA-BPP, and chlorobenzene for BPP) at 3000 r.p.m. for 30 s, and then annealed at 100 °C for 15 min. For the deposition of PTAA layer on ITO substrate, 1 mg mL$^{-1}$ PTAA toluene solution was spin-coated onto the substrate at 5000 r.p.m. for 30 s, and then annealed at 120 °C for 20 min. Subsequently, a solution with 1.35 M PbI$_2$ and 0.0675 M CsI dissolved in DMF/DMSO (19:1, v/v) was spin-coated on the substrate at 3000 r.p.m. for 30 s in the N$_2$ glove box. Next, a mixed organic cation solution (60 mg FAI, 20 mg MAI, and 5 mg MACl dissolved in 1 ml isopropanol) was spin-coated at 3000 r.p.m. for 30 s and then annealed at 150 °C for 10 min, which formed a triple-cation Cs$_{0.05}$(FA$_{0.78}$MA$_{0.22}$)$_{0.95}$PbI$_3$ perovskite layer according to the previous study.[26] After that, 5 mg ml$^{-1}$ PCBM chlorobenzene solution was spin-coated on the perovskite surface at 1000 r.p.m. for 30 s and annealed at 70 °C for 10 min. Finally, 20 nm C$_{60}$, 5 nm BCP, and 80 nm Ag electrodes were evaporated onto the substrate sequentially under a vacuum condition of 10$^{-7}$ Torr.

*Fabrication of Perovskite Solar Modules*: The perovskite solar module consisted of seven subcells connected in series on a $5 \times 5$ cm$^2$ ITO substrate. There P1 pattern of ITO substrate was designed by the Yingkou OPV Tech New Energy. The ITO substrate with P1 pattern was cleaned and then deposited with a hole-selective layer by using the spin-coating method described above. The perovskite layers were spin-coated onto the $5 \times 5$ cm$^2$ substrates based on the same sequential deposition method for the small-sized PSCs, followed by a two-step annealing process at 90 and 150 °C for 1 and 10 min, respectively. After the deposition of PCBM and C$_{60}$ layers, the samples were etched by a picosecond laser (Picosecond Laser Processing System, LPS-R002A, Spectronix Corporation), a 532 nm wavelength laser (power of 3.0 W) with a pulse duration of 12 ps is applied to create the P2 pattern. Subsequently, 5 nm of compact tin oxide layer was deposited on the C$_{60}$ surface via an atomic layer deposition system (Cambridge Nanotechnology, Savannah S200) at low temperature, tetrakis(dimethylamino)tin(IV) was chosen as the tin source and the growth rate of the ALD-SnO$_2$ layer was fixed at 0.53 Å per cycle. Then, the samples were transferred into a high-vacuum chamber and 80 nm Ag electrode was evaporated onto the ALD-SnO$_2$ layer. Finally, the laser with a power of 3.8 W was used to form the P3 pattern after evaporation of Ag.

*Characterization of PSC Performance*: The device $J$–$V$ curves were measured under AM1.5G light illumination (100 mW cm$^{-2}$, calibrated by a KG3 reference silicon cell (Enlitech)) using a solar simulator (Newport Oriel Sol 1A, xenon lamp, USHIO, UXL-150SO) and Keithley 2420 source meter without preconditioning at room temperature and a relative humidity of 30%. For the small-sized cells, the $J$–$V$ scan range was from −0.1 to 1.2 V and a metal mask with an aperture area of 0.1 cm$^2$ was used for the measurement. For $5 \times 5$ cm$^2$ solar modules, the $J$–$V$ scan range was from −0.1 to 8.5 V and a mask with an aperture area of 22.4 cm$^2$ was used for the measurement. The IPCE spectra of the inverted PSCs were characterized using Oriel IQE 200 system.

Other characterizations of the small molecules and thin films, the data processing details, and the DFT calculation details were summarized in the Supporting Information.

## Supporting Information

Supporting Information is available from the Wiley Online Library or from the author.

## Conflict of Interest

The authors declare no conflict of interest.

## Author Contributions

T.W. and X.X. contributed equally to this work. Y.B.Q. and A.N. supervised this research project. T.W., Y.B.Q., X.X., and A.N. conceived the experiments, performed the data analysis, and wrote the draft manuscript. T.W., X.X., L.H., S.Y., A.N., and Y.B.Q. participated in the discussion about the experimental details. X.X., S.R., and Q.Z. synthesized the molecules. T.W. and J.Z. conducted the solar cell fabrication. T.W. and T.G. performed the theoretical calculations. K.M. helped with the transient absorption spectroscopy measurements. L.K.O., K.M., S.Y., P.J., X.L., H.S., C.Z., S.M., T.L., and C.D. helped with the sample preparation for characterization. T.W., L.K.O., S.M., C.Z., and R.K. conducted the characterization. All authors contributed to revising the paper.

## Data Availability Statement

The data that support the findings of this study are available from the corresponding author upon reasonable request.

## Keywords

graphene-like conjugated molecule, hole-selective contact, inverted perovskite solar cell, operational stability, solar module

[1] S. Chen, X. Dai, S. Xu, H. Jiao, L. Zhao, J. Huang, *Science* **2021**, *373*, 902.

[2] T. Bu, L. K. Ono, J. Li, J. Su, G. Tong, W. Zhang, Y. Liu, J. Zhang, J. Chang, S. Kazaoui, F. Huang, Y. B. Cheng, Y. B. Qi, *Nat. Energy* **2022**, *7*, 528.

[3] T. Wu, Z. Qin, Y. Wang, Y. Wu, W. Chen, S. Zhang, M. Cai, S. Dai, J. Zhang, J. Liu, Z. Zhou, X. Liu, H. Segawa, H. Tan, Q. Tang, J. Fang, Y. Li, L. Ding, Z. Ning, Y. B. Qi, Y. Zhang, L. Han, *Nano-Micro Lett.* **2021**, *13*, 152.

[4] Z. Li, B. Li, X. Wu, S. A. Sheppard, S. Zhang, D. Gao, N. J. Long, Z. Zhu, *Science* **2022**, *376*, 416.

[5] Y. Gao, R. Lin, K. Xiao, X. Luo, J. Wen, X. Yue, H. Tan, *Joule* **2022**, *6*, 1944.

[6] R. Lin, J. Xu, M. Wei, Y. Wang, Z. Qin, Z. Liu, J. Wu, K. Xiao, B. Chen, S. M. Park, G. Chen, H. R. Atapattu, K. R. Graham, J. Xu, J. Zhu, L. Li, C. Zhang, E. H. Sargent, H. Tan, *Nature* **2022**, *603*, 73.

[7] D. Zhao, C. Chen, C. Wang, M. M. Junda, Z. Song, C. R. Grice, Y. Yu, C. Li, B. Subedi, N. J. Podraza, X. Zhao, G. Fang, R. G. Xiong, K. Zhu, Y. Yan, *Nat. Energy* **2018**, *3*, 1093.

[8] X. Li, W. Zhang, X. Guo, C. Lu, J. Wei, J. Fang, *Science* **2022**, *375*, 434.

[9] J. Zhang, J. Yang, R. Dai, W. Sheng, Y. Su, Y. Zhong, X. Li, L. Tan, Y. Chen, *Adv. Energy Mater.* **2022**, *12*, 2103674.

[10] K. Yang, Q. Liao, J. Huang, Z. Zhang, M. Su, Z. Chen, Z. Wu, D. Wang, Z. Lai, H. Y. Woo, *Angew. Chem., Int. Ed.* **2022**, *134*, 202113749.

[11] Y. Yao, C. Cheng, C. Zhang, H. Hu, K. Wang, S. De Wolf, *Adv. Mater.* **2022**, *34*, 2203794.

[12] R. Li, C. Li, M. Liu, P. Vivo, M. Zheng, Z. Dai, J. Zhan, B. He, H. Li, W. Yang, Z. Zhou, H. Zhang, *CCS Chem.* **2022**, *4*, 3084.

[13] S. Huang, Z. Liu, J. Xu, D. Zhang, H. Dong, Z. Wu, L. Duan, *Chem. Eng. J.* **2022**, *430*, 132986.

[14] H. Liu, K. Yan, J. Rao, Z. Chen, B. Niu, Y. Huang, H. Ju, B. Yan, J. Yao, H. Zhu, H. Chen, C. Z. Li, *ACS Appl. Mater. Interfaces* **2022**, *14*, 6794.

[15] X. Wang, K. Rakstys, K. Jack, H. Jin, J. Lai, H. Li, C. S. K. Ranasinghe, J. Saghaei, G. Zhang, P. L. Burn, I. R. Gentle, P. E. Shaw, *Nat. Commun.* **2021**, *12*, 52.

[16] Y. Chen, Y. shen, W. Tang, Y. Wu, W. Luo, N. Yuan, J. Ding, S. Zhang, W. H. Zhang, *Adv. Funct. Mater.* **2022**, *32*, 2206703.

[17] D. Ouyang, C. Chen, Z. Huang, L. Zhu, Y. Yan, W. C. H. Choy, *ACS Appl. Mater. Interfaces* **2021**, *13*, 16611.

[18] H. Chen, Q. Wei, M. I. Saidaminov, F. Wang, A. Johnston, Y. Hou, Z. Peng, K. Xu, W. Zhou, Z. Liu, L. Qiao, X. Wang, S. Xu, J. Li, R. Long, Y. Ke, E. H. Sargent, Z. Ning, *Adv. Mater.* **2019**, *31*, 1903559.

[19] T. Wu, X. Li, Y. Qi, Y. Zhang, L. Han, *ChemSusChem* **2021**, *14*, 4354.

[20] M. Jeong, I. W. Choi, K. Yim, S. Jeong, M. Kim, S. J. Choi, Y. Cho, J. H. An, H. B. Kim, Y. Jo, S. H. Kang, J. H. Bae, C. W. Lee, D. S. Kim, C. Yang, *Nat. Photonics* **2022**, *16*, 119.

[21] J. Wang, Z. Yu, D. D. Astridge, Z. Ni, L. Zhao, B. Chen, M. Wang, Y. Zhou, G. Yang, X. Dai, A. Sellinger, J. Huang, *ACS Energy Lett.* **2022**, *7*, 3353.

[22] A. Al-Ashouri, E. Köhnen, B. Li, A. Magomedov, H. Hempel, P. Caprioglio, J. A. Márquez, A. B. Morales Vilches, E. Kasparavicius, J. A. Smith, N. Phung, D. Menzel, M. Grischek, L. Kegelmann, D. Skroblin, C. Gollwitzer, T. Malinauskas, M. Jošt, G. Matič, B. Rech, R. Schlatmann, M. Topič, L. Korte, A. Abate, B. Stannowski, D. Neher, M. Stolterfoht, T. Unold, V. Getautis, S. Albrecht, *Science* **2020**, *370*, 1300.

[23] A. Ullah, K. H. Park, H. D. Nguyen, Y. Siddique, S. F. A. Shah, H. Tran, S. Park, S. I. Lee, K. K. Lee, C. H. Han, K. Kim, S. Ahn, I. Jeong, Y. S. Park, S. Hong, *Adv. Energy Mater.* **2022**, *12*, 2103175.

[24] Y. Wang, H. Ju, T. Mahmoudi, C. Liu, C. Zhang, S. Wu, Y. Yang, Z. Wang, J. Hu, Y. Cao, F. Guo, Y. B. Hahn, Y. Mai, *Nano Energy* **2021**, *88*, 106285.

[25] Y. Wang, L. Duan, M. Zhang, Z. Hameiri, X. Liu, Y. Bai, X. Hao, *Sol. RRL* **2022**, *6*, 2200234.

[26] T. Wu, L. K. Ono, R. Yoshioka, C. Ding, C. Zhang, S. Mariotti, J. Zhang, K. Mitrofanov, X. Liu, H. Segawa, R. Kabe, L. Han, Y. B. Qi, *Energy Environ. Sci.* **2022**, *15*, 4612.

[27] X. Zheng, Y. Deng, B. Chen, H. Wei, X. Xiao, Y. Fang, Y. Lin, Z. Yu, Y. Liu, Q. Wang, J. Huang, *Adv. Mater.* **2018**, *30*, 1803428.

[28] X. Dai, Y. Deng, C. H. Van Brackle, S. Chen, P. N. Rudd, X. Xiao, Y. Lin, B. Chen, J. Huang, *Adv. Energy Mater.* **2020**, *10*, 1903108.

[29] R. Chen, S. Liu, X. Xu, F. Ren, J. Zhou, X. Tian, Z. Yang, X. Guanz, Z. Liu, S. Zhang, Y. Zhang, Y. Wu, L. Han, Y. B. Qi, W. Chen, *Energy Environ. Sci.* **2022**, *15*, 2567.

[30] A. Al-Ashouri, A. Magomedov, M. Roß, M. Jošt, M. Talaikis, G. Chistiakova, T. Bertram, J. A. Márquez, E. Köhnen, E. Kasparavičius, S. Levcenco, L. Gil-Escrig, C. J. Hages, R. Schlatmann, B. Rech, T. Malinauskas, T. Unold, C. A. Kaufmann, L. Korte, G. Niaura, V. Getautis, S. Albrecht, *Energy Environ. Sci.* **2019**, *12*, 3356.

[31] E. Aktas, N. Phung, H. Köbler, D. A. González, M. Méndez, I. Kafedjiska, S. H. Turren-Cruz, R. Wenisch, I. Lauermann, A. Abate, E. Palomares, *Energy Environ. Sci.* **2021**, *14*, 3976.

**ADVANCED
SCIENCE NEWS**

www.advancedsciencenews.com

**ADVANCED
MATERIALS**

www.advmat.de

[32] S. Zhang, R. Wu, C. Mu, Y. Wang, L. Han, Y. Wu, W. H. Zhu, *ACS Mater. Lett.* **2022**, *4*, 1976.

[33] H. Su, T. Wu, D. Cui, X. Lin, X. Luo, Y. Wang, L. Han, *Small Methods* **2020**, *4*, 2000507.

[34] N. Balis, E. Stratakis, E. Kymakis, *Mater. Today* **2016**, *19*, 580.

[35] A. Narita, X. Y. Wang, X. Feng, K. Müllen, *Chem. Soc. Rev.* **2015**, *44*, 6616.

[36] W. Chen, F. Yu, Q. Xu, G. Zhou, Q. Zhang, *Adv. Sci.* **2020**, *7*, 1903766.

[37] R. Scholl, H. Neumann, *Ber. Deutsch. Chem.* **1922**, *55*, 118.

[38] E. Clar, *Chem. Ber.* **1939**, *72*, 1645.

[39] D. Lungerich, O. Papaianina, M. Feofanov, J. Liu, M. Devarajulu, S. I. Troyanov, S. Maier, K. Amsharov, *Nat. Commun.* **2018**, *9*, 4756.

[40] X. Xu, S. Gunasekaran, S. Renken, L. Ripani, D. Schollmeyer, W. Kim, M. Marcaccio, A. Musser, A. Narita, *Adv. Sci.* **2022**, *9*, 2200004.

[41] C. Li, J. Wei, M. Sato, H. Koike, Z. Z. Xie, Y. Q. Li, K. Kanai, S. Kera, N. Ueno, J. X. Tang, *ACS Appl. Mater. Interfaces* **2016**, *8*, 11526.

[42] T. Wu, X. Liu, X. He, Y. Wang, X. Meng, T. Noda, X. Yang, L. Han, *Sci China Chem* **2020**, *63*, 107.

[43] Y. N. Lu, J. X. Zhong, Y. Yu, X. Chen, C. Y. Yao, C. Zhang, M. Yang, W. Feng, Y. Jiang, Y. Tan, L. Gong, X. Wei, Y. Zhou, L. Wang, W. Q. Wu, *Energy Environ. Sci.* **2021**, *14*, 4048.

[44] T. J. Miao, J. Tang, *J. Chem. Phys.* **2020**, *152*, 194201.

[45] J. Oh, S. M. Lee, S. Jung, J. Lee, G. Park, S. H. Kang, Y. Cho, M. Jeong, B. Lee, S. Kim, C. Yang, *Sol. RRL* **2021**, *5*, 2000812.

[46] L. Calio, S. Kazim, M. Graetzel, S. Ahmad, *Angew. Chem., Int. Ed.* **2016**, *55*, 14522.

[47] T. Wu, Y. Wang, Z. Dai, D. Cui, T. Wang, X. Meng, E. Bi, X. Yang, L. Han, *Adv. Mater.* **2019**, *31*, 1900605.

[48] M. L. Agiorgousis, Y. Y. Sun, H. Zeng, S. Zhang, *J. Am. Chem. Soc.* **2014**, *136*, 14570.

[49] J. He, W. H. Fang, R. Long, O. V. Prezhdo, *Nano Energy* **2021**, *79*, 105491.

[50] E. J. Juarez-Perez, L. K. Ono, Y. B. Qi, *J. Mater. Chem. A* **2019**, *7*, 16912.

[51] E. J. Juarez-Perez, Z. Hawash, S. R. Raga, L. K. Ono, Y. B. Qi, *Energy Environ. Sci.* **2016**, *9*, 3406.

[52] L. Shi, M. P. Bucknall, T. L. Young, M. Zhang, L. Hu, J. Bing, D. S. Lee, J. Kim, T. Wu, N. Takamure, D. R. McKenzie, S. Huang, M. A. Green, A. W. Y. Ho-Baillie, *Science* **2020**, *368*, aba2412.

[53] D. Wei, F. Ma, R. Wang, S. Dou, P. Cui, H. Huang, J. Ji, E. Jia, X. Jia, S. Sajid, A. M. Elseman, L. Chu, Y. Li, B. Jiang, J. Qiao, Y. Yuan, M. Li, *Adv. Mater.* **2018**, *30*, 1707583.

[54] E. Bi, W. Tang, H. Chen, Y. Wang, J. Barbaud, T. Wu, W. Kong, P. Tu, H. Zhu, X. Zeng, J. He, S. Kan, X. Yang, M. Grätzel, L. Han, *Joule* **2019**, *3*, 2748.

[55] X. Xu, A. L. Vonder Haar, R. Yoshioka, Q. Zhang, S. Vasylevskyi, A. J. Musser, A. Narita, *Chem. Commun.* **2023**, *59*, 720.